



CHORUS

This is the accepted manuscript made available via CHORUS. The article has been published as:

Plasma Collision in a Gas Atmosphere

S. Le Pape, L. Divol, G. Huser, J. Katz, A. Kemp, J. S. Ross, R. Wallace, and S. Wilks

Phys. Rev. Lett. **124**, 025003 — Published 15 January 2020

DOI: [10.1103/PhysRevLett.124.025003](https://doi.org/10.1103/PhysRevLett.124.025003)

Plasma collision in a gas atmosphere

S. Le Pape,¹ L. Divol,¹ G. Huser,² J. Katz,³ A. Kemp,¹ J.S. Ross,¹ R. Wallace,¹ and S. Wilks¹

¹*Lawrence Livermore National Laboratory, Livermore, CA 94550, USA*

²*CEA, DAM, DIF, Bruyeres-le-Chatel, F-91297 Arpajon, France*

³*Laboratory for Laser Energetics, University of Rochester,
250 East River Road, Rochester, New York 14623, USA*

(Dated: December 10, 2019)

We present a study on the impact of a gas atmosphere on the collision of two counter propagating plasmas (gold and carbon). Imaging optical Thomson scattering data of the plasma collision with and without helium in between have been obtained on the Omega laser facility. Without gas, we observed large scale mixing of colliding gold and carbon ions. Once ambient helium is added, the two plasmas remain separated. The difference in ionic temperature is consistent with a reduction of the maximum Mach number of the flow from $M=7$ to $M=4$. It results in a reduction of a factor ~ 10 of the counter-streaming ion-ion mean free path. By adding a low density ambient gas, it is possible to control the collision of two high velocity counter streaming plasma, transitioning from an interpenetrating regime to a regime in agreement with a hydrodynamic description.

PACS numbers: 52.50.Jm, 52.25.Os, 52.27.Gr, 52.65.Yy

Plasma collisions can have very different characteristics depending on conditions. At low-density, a plasma collision can lead to the formation of collisionless shocks [1],[2] that are thought to be the source of magnetic fields and particle acceleration to cosmic ray energies. At higher density, it can lead to the formation of a hot dense plasma used to generate X-ray lasers [3],[4]. Colliding plasma are also a key feature in inertial fusion chambers where the chamber walls are exposed to extreme flux, expected to generate stagnation of plasma clouds that could limit the lifetime of inertial fusion chambers [5], [6]. In Inertial Confinement Fusion (ICF), a low Z capsule containing the DT fuel is ablatively driven by X ray emanating from the interaction of a high Z cylinder (hohlraum) and a high energy laser. The ablated hohlraum wall can collide with the expanding plasma from the compressed capsule[7]. Controlling this collision is important for sustaining laser ignition pulses.

Previous studies of high velocity plasma collisions in vacuum have shown ballistic or diffusive interpenetration[8],[9]. The mixing of the counterstreaming plasma species was only limited by the size of the system or by electrostatic/magnetic instabilities[10],[2]. On the other hand, the back pressure provided by a high density ambient gas can slow down the expansion of a laser driven plasma, allowing control of stagnation in ICF systems, but restricting the laser propagation and coupling to the target [11],[12]. In addition, proton radiography of the gas interface have shown a wide mixing layer attributed to Rayleigh-Taylor (RT) instabilities growth seeded by non-uniformity in laser illumination as the expanding plasma slows down in the gas[13].

In this paper, we report on the successful control of plasma expansions and stagnation by using a low density/low Z ambient gas. Imaging Thomson Scattering (TS) is used to fully characterize the collision of laser

driven gold and carbon plasmas. In the vacuum case, we observe mixing of the ions over the entire field of view, along with strong ion heating, consistent with previous studies[8]. When an ambient helium density of 0.15 mg/cm^3 ($n_e=0.003\%$ of the laser critical density) is added, the carbon and gold ions remains separated with an interface mix width $< 50 \mu\text{m}$ (instrumental resolution of the TS diagnostic) and much less ion heating. At this low density, the helium plasma does not provide much back pressure that could lead to RT instabilities (as it is measured to diffuse through the gold and carbon plasmas), but limits the electrostatic potential and acceleration of the front of the plasma expansions. Paradoxically the presence of a kinetic agent (a low density helium plasma) keeps the system amenable to a hydrodynamic description. This regime, where the helium gas does not alter the laser beam propagation, is the regime of choice for current attempts at controlling ICF implosions on the NIF.

An experiment was carried out on the Omega laser facility [15] to measure the plasma conditions using Optical Thomson Scattering. The target (figure 1-a) is composed of a gold band, 1.6 mm in radius, $800 \mu\text{m}$ in length and $25 \mu\text{m}$ thick, and a High Density Carbon puck (HDC, $\rho= 3.45 \text{ g/cm}^3$) $600 \mu\text{m}$ in radius and $800 \mu\text{m}$ in length positioned at the gold band center. To study the impact of helium on the plasma collision, the target is placed inside a gasbag filled with 0.15 mg/cm^3 of He4. A gasbag consists of an aluminum washer of inner diameter 4 mm with a thin polyimide (C22H10N2O4) skin bonded to each end. When inflated, a gasbag forms an oblate ellipsoid $\sim 5.5\text{mm}$ long, with a skin thickness of $0.35\text{-}0.4 \mu\text{m}$ (figure 1-b). Omega laser beams are focused on the gold and HDC surfaces using phase plates resulting in a $300 \mu\text{m}$ focal spot. Nineteen laser beams at $\lambda_{3\omega}=351\text{-nm}$ were focused on the inside of the gold surface, nine

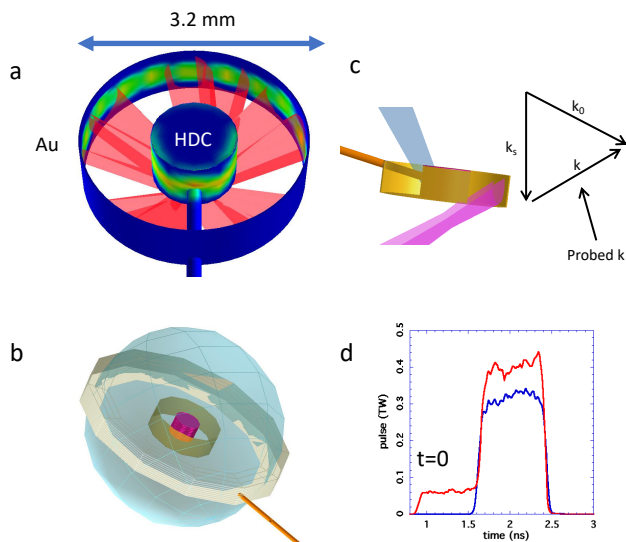


FIG. 1. a) Schematic of the target for the Gold/Carbon case. On the target surfaces the laser intensity is shown as calculated by a 3-D thermal radiation and CAD code (VIS-RAD [14]), only a subset of laser beams are shown for clarity. b) Schematic of the gasbag target. c) Geometry of the Thomson probe. d) blue: laser pulse shape used without the helium gas bag, red: laser pulse shape used with the helium gas bag.

beams were focused on the surface of the HDC puck. The beam pointing was optimized to reduce intensity variation on the target surface preventing the apparition of pronounced jets emanating from the space between two cluster of laser spots [16].

For the vacuum shot, i.e no gas bag, each beam had 300 J in a 1-ns flat top pulse (figure 1-d) leading to an intensity on the target surfaces of $4 \times 10^{14} \text{W/cm}^2$. When a gas bag was used each beam has 370 J in a stepped pulse with 300 J in a 1-ns flat top pulse (figure 1-d). The Thomson-scattering diagnostic [17],[18],[19],[20] consisted of a 40-J, 1-ns-long, $\lambda_{4\omega} = 263.23\text{-nm}$ probe beam with a best-focus diameter of $\sim 50 \mu\text{m}$ [21]. The intensity of the probe beam, reached at its best focus, is low enough to stay below the Filamentation Figure of Merit (FFOM) defined in [22] in our plasma (1 keV electron temperature at 4ω) and focusing conditions ($f_{\text{number}} = 10$).

The light scattered from a $50 \mu\text{m} \times 50 \mu\text{m} \times 1000 \mu\text{m}$ volume was imaged through a 1/3-m spectrometer. Spatially resolved Thomson-scattering measurements are made by aligning the image of the probe beam parallel to the spectrometer input slit ($100 \mu\text{m}$ wide) and recording the spectrally dispersed image on a CCD. The spectral dispersion was 0.411 nm/pxl , the scattering angle 60 degree (figure 1-c). The Thomson scattering data is taken at the end of the main laser pulse (figure 1-d) for a $\sim 300 \text{ps}$ duration.

Spatially resolved Thomson Scattering (TS) spectra

are shown on the figure 2-a for the gold/carbon case and figure 2-e for the gold/helium/carbon case. Figures 2-b,c,d and 2-f,g,h show spectral line-outs for the two cases. The flow velocity can be measured from the Doppler shift of the midpoint of the Thomson scattered signal. The velocities of the carbon and gold flow have opposite directions [23] (figure 4-b) leading to red-shifted or blue-shifted spectra. The wavelength separation of the two ionic peaks is related to the sound speed which is proportional to $\sqrt{\frac{ZT_e + 3T_i}{M_i}}$, where T_e is the electron temperature, T_i the ion temperature and M_i the ion mass and Z the ionization state. Here we assumed fully ionized carbon $Z=6$ and $Z=45$ [24] for gold and the ionic peak separation allows the determination of the electron temperature (T_e) when $\frac{T_i}{ZT_e}$ is small. Ionic Landau damping [25, 26], when $\frac{T_i}{ZT_e}$ is sizable, broadens the ionic peak enabling the determination of the ion temperature. Throughout this paper the TS spectra are fitted using a multi-species, multi-flow kinetic model for the plasma dispersion, which usually allows a determination of the temperature and average flow velocity for each species [27]. The TS power is expressed by using the spectral density function with two ion species i :

$$S(k, \omega) = (2\pi/k) |\chi_e/\epsilon|^2 \sum_i (Z_i^2 n/n_e) f_{i0}((\omega + k \cdot v_d)/k),$$

where $\omega = \omega_s - \omega_0$, ω_s and ω_0 are the frequency of the scattered light and TS probe, respectively, n is the density of each ion species, v_d is the drift velocity, ϵ is the dielectric function and χ_e the electron susceptibility, f_{i0} is the ion velocity distribution function and Z_i is the average charge state.

In the vacuum case, the entire plasma at the time of the measurement is a hot mix of gold and carbon ions, the two counter-streaming plasmas having interpenetrated (Fig. 2-a). When a low density (0.15 mg/cm^3) ambient helium gas is added, a narrow ($\sim 50 \mu\text{m}$) cold mix layer separates the gold plasma from the carbon plasma (Fig. 2-e), with the He ions diffusing across the boundary. From the line-outs on figure 2 more detailed data on the plasma conditions can be extracted. At the $200 \mu\text{m}$ position near the gold wall (figure 2-b,f), ion gold peaks are observed in both cases. In the gold/carbon case, a blue-shifted tail and an asymmetry of the ionic peak can be observed, indicative of fast carbon ions having reached this position. In the gold/helium/carbon case, only one gold peak is observed. In the gold plasma (figure 2 d-f) the symmetry of the ion peaks is affected by Landau damping induced by light ions mixing (helium or carbon). The blue shifted peak is totally suppressed in the gold helium case. At the $400 \mu\text{m}$ position (figure 2 c,g), the gold/carbon case shows a broad single peak while the gold/helium/carbon case shows two separated carbon peaks. The broad ionic peak observed is due to the presence of hot ($> 20 \text{keV}$) gold and carbon ions in the

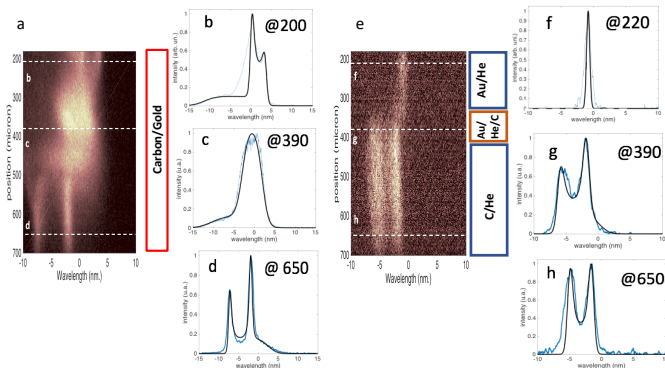


FIG. 2. a) Spatially resolved Thomson scattering spectra in the Gold/Carbon case. b,c,d) blue curves: Line outs over figure 2-a at various positions along the spatial axis, distances are measured from the Au surface. Black curve: theoretical fits to experimental data e) Spatially resolved Thomson scattering spectra in the Gold/helium Carbon case. f,g,h) blue curves: Line outs over figure 2-e at various positions along the spatial axis, distances are measured from the Au surface. Black curve: theoretical fits to experimental data

same region. The two asymmetric carbon ion peaks observed are due to the presence of cold ($< 1keV$) carbon mixed with cold ($< 1keV$) helium ion. At the $650\mu m$ position (figure 2 d,h), in the gold/carbon case, two carbon peaks are observed with a blue-shifted tail indicative of the presence of fast gold ions. At the same position in the gold/helium/carbon case, no tail is observed with almost symmetric carbon peaks, indicative of a pure carbon plasma with a trace of helium.

From similar fits at various positions along the space axis, the temperature (ion and electron) and species fraction profile can be inferred (figure 3). Figure 3-a-b shows the ion species fraction for the two cases, where the transition from a sharp separation of the two fluids by a narrow mixing layer when ambient He is added to a uniformly hot mixed plasma in the vacuum case is clear. In the Au/C case, gold is present throughout the field of view, at an atomic fraction ranging from 5×10^{-2} , $200\mu m$ away from the gold wall to $\sim 10^{-3}$, $300\mu m$ away from the carbon puck. In the Au/He/C case, gold is only present in the first $300\mu m$ from the gold wall, along with helium at about 50/50 ratio. From $350\mu m$ to the carbon puck, only carbon and helium are present, with a helium fraction ranging from 0.5 to about zero next to the carbon puck. Figure 3-c,d show the temperature profile for the two cases. In the Au/C case the ion temperature of the carbon is $\sim 20 keV$ where the gold species fraction is above 10^{-3} , while it stays below $1 keV$ everywhere when ambient He is added. Very close to the carbon puck, the carbon temperature is similar in both cases, around $1 keV$, as the ablation physics is dominated by laser absorption.

Time resolved data (the scattered signal is imaged onto

a optical streak camera) over a $50\mu m$ cube volume at the $400\mu m$ spatial position are shown on figure 4 for the Au/C case using the same laser drive (300J per laser beam). The Thomson probe was on for 1 ns, starting 300 ps after the beginning of the main laser driver. The flow velocities of the two species decrease in time as the ion temperature of the two species increases implying a transfer from the kinetic energy of the counter-streaming flows into thermal energy through Coulomb collisions[8]. Time resolved and spatially resolved data are consistent (spatial data are taken at 1 ns for 300 ps). Carbon ion temperature is already at $\sim 10keV$ at 0.9 ns. The ion concentration of the two species is also measured as a function of time. At 300 ps the gold and carbon are already mixed, which explains the high gold ion temperature ($\sim 20 keV$). By 600 ps, the gold starts to push the carbon away from the probed zone leading to a decrease in the carbon ion density. At all times the plasma is mostly composed of carbon ions with a small fraction ($< 1\%$) of gold ions, similar to the late-time spatially resolved data at this probed position.

The large differences in ion temperature reached for the two cases (tens of keV for the Au/C case, $\sim 1 keV$ for the Au/He/C), in mix layer width and composition can be explained by the strong slowdown of the front of a plasma expansion in vacuum in the presence of a low density ambient plasma. For the Au/C case, the early laser driven expansion of the gold (and carbon) can be approximated by a self-similar isothermal expansion [9] for the electron density $N_e = N_0 * exp(-(\xi + 1))$ and flow velocity $v_i = C_s(\xi + 1)$, where $\xi = \frac{x}{C_s t}$, N_0 is the critical density for a 32 degree angle of incidence and $C_s = \sqrt{\frac{\gamma Z K_b T_e}{M_i}}$ is the ion sound speed (here the ion sound speed is calculated for $T_e = 1keV$, $Z=45$ for gold ions cf fig 4.a, $C_S \sim 1.9 \times 10^7 cm/s$). In a self-similar description, the flow velocity increases indefinitely with time and space. This description breaks down when the Debye length equals the density scale length $C_S t$ [28] due to charge separation effects. The maximum ion front velocity is then given by [29] $v_{front} = 2C_S \ln(2\tau)$, where $\tau = \frac{\omega_{pi} t}{\sqrt{2e}}$, ω_{pi} being the ion plasma frequency at N_0 ; at 300 ps we calculate $\tau = 7.5 \times 10^3$ which gives a peak velocity of the gold ions $v_{front} \sim 3.6 \times 10^8 cm/s$, a Mach number $M \sim 19$. The electron density at $M=19$ following the same description is $\sim 3.5 \times 10^{13}$, well below the detection threshold of our diagnostic. Experimentally, from time resolved data, the fastest detected gold ions have reached the Thomson volume located $400\mu m$ from their initial position is 300ps. It corresponds to a velocity of $\sim 1.3 \times 10^8 cm/s$, which is about $M=7$ at a measured electron density of $2 \times 10^{19} cm^{-3}$, which is higher than the density inferred from the self-similar expansion at $M=7$ ($n_e \sim 6 \times 10^{18}$). Figure 4 shows that the ion temperature at 300ps is already high ($> 2 keV$), suggesting that the gold ions have already slowed down on the carbon

leading to a higher ion density.

In the gold/helium/carbon case, the ion front velocity is not limited by space charge effects but by the density of the helium at the gold/helium interface [30]. This interface is a contact discontinuity, where pressure and velocity are continuous. The laser will maintain a continuous electron temperature. Assuming fully ionized He, $Z = 45$ for Au and $T_{Au} \sim T_{He} \sim T_e$ near the interface as measured (Fig.3-d), equating pressures $P = N_e(T_e + T_i/Z)$ on both sides leads to $N_e(Au) = 3/2N_e(He)$. Laser-heated helium is weakly shocked by the gold expansion, and one can finally assume for this estimate that $N_e(Au) \sim 1 \times 10^{20} \text{ cm}^{-3}$, roughly twice the initial gas density. 0.15 mg/cm^3 of helium is transparent for the laser, one can then assume that the self-similar expansion near the ablation front is comparable for both the helium and the vacuum case. The peak gold ion velocity, set by the helium density at the Au/He interface, would have then a Mach number $\sim M = 4$, much less than in the vacuum case.

This difference in peak velocity of the gold ions has a significant impact on their mean free path through counter streaming carbon. The ion-ion mean free path of a supersonic flow into a counter propagating flow scales as the fourth power of the relative velocity of the two flows[31]. From the vacuum to the helium case, the peak velocity of the gold ions decreases by a factor 1.75 which is a factor of ~ 10 in mean free path. From the conditions measured at 300 ps in the vacuum case (cf fig 4), the relative flow velocity is $\sim 10^8 \text{ cm/s}$, the ion density is $\sim 5 \times 10^{19} \text{ cm}^{-3}$, the mean free path of a gold ion into carbon is about $\sim 500 \mu\text{m}$ for the vacuum case reduced to $50 \mu\text{m}$ with ambient helium. This is consistent with the observed thickness of the mix layer in that case. The origin of a gold/helium mix layer in high ambient gas fill density experiment was hypothesized to be the growth of Rayleigh-Taylor instabilities at the gold helium interface. In this experiment, the initial gas electron density is ~ 20 times less than the gas electron density used in previous experiments[13], resulting in an helium fully mix with carbon and gold thus not slowing down the expanding gold. In addition RT seeds were strongly reduced by optimizing the geometry of irradiation. In addition, in the vacuum case, we can observe the presence of gold mixed with carbon over hundred's of microns which is incompatible with RT growth rate (too early). We cannot completely rule out RT instabilities as the cause of the $\sim 50 \mu\text{m}$ mix layer observed in the helium case, but the physical differences of the two systems as well as our experimental observations do not point to RT instabilities as the source of the observed mix.

This experiment was designed to emulate the plasma conditions of a near vacuum to low gas fill He-filled hohlraum used on the National Ignition Facility (NIF). The laser intensity on the wall of the Omega target is in the same range ($4 \times 10^{14} \text{ W/cm}^2$) as the intensity reached

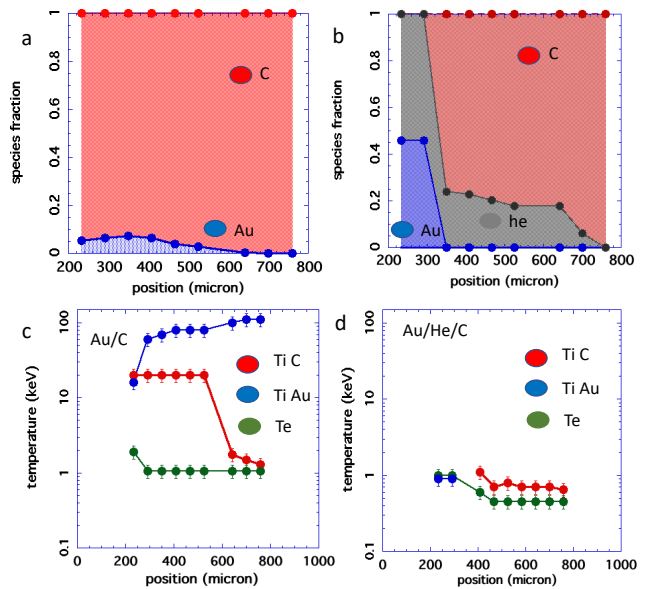


FIG. 3. Zero is the initial position of the gold ring, thousand is the initial position of the carbon puck for all four plots. a) species fraction for the gold/carbon case as a function of space. b) species fraction for the gold/helium/carbon case as a function of space. c) Temperature (ion and electron) the gold/carbon case as a function of space. d) Temperature (ion and electron) the gold/helium/carbon case as a function of space.

on the NIF hohlraum walls. We can now explain the surprising transition observed on the NIF when the helium density was lowered below 0.3 mg/cm^3 to 0.03 mg/cm^3 . Our Omega results suggest that at 0.3 mg/cm^3 helium fill, the plasma ablated from the hohlraum gold wall and the carbon capsule remain mostly separated while they would mixed over large scale length in the near vacuum case. These changes in plasma conditions with helium fill density can explain the disagreement between Radiation-hydrodynamic simulations [32] and experimental data [33] observed in the NVH case and the overall good agreement at 0.3 g/cm^3 [34],[35].

In conclusion, we report on a direct measurement of the impact of a gas atmosphere on the collision of two laser ablated counter-propagating plasmas. Spatially and time resolved optical Thomson scattering data show that the presence of a low density helium (0.003% of the laser critical density) limits the peak velocity of the expanding ion flows. A clear transition is observed when gas is added, from large scale ion mixing to two plasmas separated by a narrow mixing layer. This drastically changes plasma parameters throughout the system as observed in this letter. The strong impact of a low density gas fill on plasma collisions should enable control of implosion in low gas fill ICF hohlraums.

The author would like to thank A.J. Mackinnon and N.B. Meezan for the insightful discussions and help. This

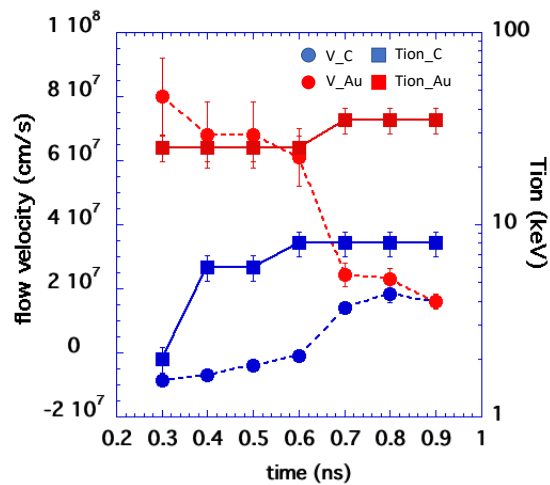


FIG. 4. The gold/carbon case, data were taken 400 m from the Au surface. Ion temperature and flow velocities as a function of time.

work was performed under the auspices of the U.S. Department of Energy by Lawrence Livermore National Laboratory under Contract DE-AC52-07NA27344. Work was also supported by the Laboratory Directed Research and Development Grant 11-ERD-050 and the National Laboratory User Facility and by General Atomics under Contract DE-NA0001808.

-
- [1] H. Takabe, T. N. Kato, Y. Sakawa, Y. Kuramitsu, T. Morita, T. Kadono, K. Shigemori, K. Otani, H. Nagatomo, T. Norimatsu, et al., *Plasma Physics and Controlled Fusion* **50**, 124057 (2008), URL <http://stacks.iop.org/0741-3335/50/i=12/a=124057>.
- [2] C. M. Huntington, F. Fiuza, J. S. Ross, A. B. Zylstra, R. P. Drake, D. H. Froula, G. Gregori, N. L. Kugland, C. C. Kuranz, M. C. Levy, et al., *Nature Physics* **11**, 173 EP (2015), URL <http://dx.doi.org/10.1038/nphys3178>.
- [3] T. Boehly, B. Yaakobi, D. Shvarts, D. Meyerhofer, P. Audebert, J. Wang, M. Rusotto, B. Boswell, R. Epstein, R. S. Craxton, et al., *Applied Physics B* **50**, 165 (1990), ISSN 1432-0649, URL <https://doi.org/10.1007/BF00357279>.
- [4] R. L. Berger, J. R. Albritton, C. J. Randall, E. A. Williams, W. L. Krueer, A. B. Langdon, and C. J. Hanna, *Physics of Fluids B: Plasma Physics* **3**, 3 (1991), <https://doi.org/10.1063/1.859954>, URL <https://doi.org/10.1063/1.859954>.
- [5] K. F. Al-Shboul, S. S. Harilal, S. M. Hassan, A. Hassanein, J. T. Costello, T. Yabuuchi, K. A. Tanaka, and Y. Hirooka, *Physics of Plasmas* **21**, 013502 (2014), <https://doi.org/10.1063/1.4859136>, URL <https://doi.org/10.1063/1.4859136>.
- [6] Y. Hirooka, T. Oishi, H. Sato, and K. A. Tanaka, *Fusion Science and Technology* **60**, 804 (2011), <https://doi.org/10.13182/FST11-A12484>, URL <https://doi.org/10.13182/FST11-A12484>.
- [7] P. W. Rambo and J. Denavit, *Physics of Plasmas* **1**, 4050 (1994), <https://doi.org/10.1063/1.870875>, URL <https://doi.org/10.1063/1.870875>.
- [8] C. Chenais-Popovics, P. Renaudin, O. Rancu, F. Gilleron, J.-C. Gauthier, O. Larroche, O. Peyrusse, M. Dirksmiller, P. Sondhaus, T. Missalla, et al., *Physics of Plasmas* **4**, 190 (1997), <https://doi.org/10.1063/1.872132>, URL <https://doi.org/10.1063/1.872132>.
- [9] J. Denavit, *The Physics of Fluids* **22**, 1384 (1979), <https://aip.scitation.org/doi/pdf/10.1063/1.862751>, URL <https://aip.scitation.org/doi/abs/10.1063/1.862751>.
- [10] N. C. Woolsey, Y. A. Ali, R. G. Evans, R. A. D. Grundy, S. J. Pestehe, P. G. Carolan, N. J. Conway, R. O. Dendy, P. Helander, K. G. McClements, et al., *Physics of Plasmas* **8**, 2439 (2001), <https://doi.org/10.1063/1.1351831>, URL <https://doi.org/10.1063/1.1351831>.
- [11] L. F. Berzak Hopkins, S. Le Pape, L. Divol, N. B. Meezan, A. J. Mackinnon, D. D. Ho, O. S. Jones, S. Khan, J. L. Milovich, J. S. Ross, et al., *Physics of Plasmas* **22**, 056318 (2015), <https://aip.scitation.org/doi/pdf/10.1063/1.4921151>, URL <https://aip.scitation.org/doi/abs/10.1063/1.4921151>.
- [12] O. S. Jones, C. J. Cerjan, M. M. Marinak, J. L. Milovich, H. F. Robey, P. T. Springer, L. R. Benedetti, D. L. Bleuel, E. J. Bond, D. K. Bradley, et al., *Physics of Plasmas* **19**, 056315 (2012), <https://doi.org/10.1063/1.4718595>, URL <https://doi.org/10.1063/1.4718595>.
- [13] C. K. Li, F. H. Séguin, J. A. Frenje, M. Rosenberg, R. D. Petrasso, P. A. Amendt, J. A. Koch, O. L. Landen, H. S. Park, H. F. Robey, et al., *Science* **327**, 1231 (2010), ISSN 0036-8075, <http://science.sciencemag.org/content/327/5970/1231.full.pdf>, URL <http://science.sciencemag.org/content/327/5970/1231>.
- [14] J. MacFarlane, *Journal of Quantitative Spectroscopy and Radiative Transfer* **81**, 287 (2003), ISSN 0022-4073, radiative Properties of Hot Dense Matter, URL <http://www.sciencedirect.com/science/article/pii/S0022407303000815>.
- [15] T. R. Boehly, R. S. Craxton, T. H. Hinterman, P. A. Jaanimagi, J. H. Kelly, T. J. Kessler, R. L. KREMENS, S. A. Kumpan, S. A. Letzring, R. L. McCrory, et al., *Fusion Technology* **26**, 722 (1994).
- [16] G. Huser, C. Courtois, and M.-C. Monteil, *Physics of Plasmas* **16**, 032703 (2009), <https://doi.org/10.1063/1.3099054>, URL <https://doi.org/10.1063/1.3099054>.
- [17] J. Katz, R. Boni, C. Sorce, R. Follett, M. J. Shoup, and D. H. Froula, *Review of Scientific Instruments* **83**, 10E349 (2012), <https://doi.org/10.1063/1.4733551>, URL <https://doi.org/10.1063/1.4733551>.
- [18] J. Katz, J. S. Ross, C. Sorce, and D. H. Froula, *Journal of Instrumentation* **8**, C12009 (2013), URL <https://doi.org/10.1088/1748-0221/2F8%2F12%2Fc12009>.
- [19] D. Montgomery, B. J. Albright, D. Barnak, P.-Y. Chang, J. Davies, G. Fiksel, D. Froula, J. Kline, M. MacDonald, A. Sefkow, et al., *Physics of Plasmas* **22**, 010703 (2015).
- [20] D. Froula, L. Divol, R. London, R. Berger, T. Döppner, N. Meezan, J. Ralph, J. Ross, L. Suter, and S. Glenzer,

- Physics of Plasmas **17**, 056302 (2010).
- [21] A. J. Mackinnon, S. Shiromizu, G. Antonini, J. Auerbach, K. Haney, D. H. Froula, J. Moody, G. Gregori, C. Constantin, C. Sorce, et al., Review of Scientific Instruments **75**, 3906 (2004), <https://doi.org/10.1063/1.1789247>, URL <https://doi.org/10.1063/1.1789247>.
- [22] D. H. Froula, L. Divol, N. B. Meezan, S. Dixit, J. D. Moody, P. Neumayer, B. B. Pollock, J. S. Ross, and S. H. Glenzer, Phys. Rev. Lett. **98**, 085001 (2007), URL <https://link.aps.org/doi/10.1103/PhysRevLett.98.085001>.
- [23] R. K. Follett, J. A. Delettrez, D. H. Edgell, R. J. Henchen, J. Katz, J. F. Myatt, and D. H. Froula, Review of Scientific Instruments **87**, 11E401 (2016), <https://aip.scitation.org/doi/pdf/10.1063/1.4959160>, URL <https://aip.scitation.org/doi/abs/10.1063/1.4959160>.
- [24] R. W. Lee, J. Nash, and Y. Ralchenko, Journal of Quantitative Spectroscopy and Radiative Transfer **58**, 737 (1997), ISSN 0022-4073, radiative Properties of Hot Dense Matter III, URL <http://www.sciencedirect.com/science/article/pii/S0022407397000794>.
- [25] P. Neumayer, R. L. Berger, L. Divol, D. H. Froula, R. A. London, B. J. MacGowan, N. B. Meezan, J. S. Ross, C. Sorce, L. J. Suter, et al., Phys. Rev. Lett. **100**, 105001 (2008), URL <https://link.aps.org/doi/10.1103/PhysRevLett.100.105001>.
- [26] S. H. Glenzer, C. A. Back, K. G. Estabrook, R. Wallace, K. Baker, B. J. MacGowan, B. A. Hammel, R. E. Cid, and J. S. De Groot, Phys. Rev. Lett. **77**, 1496 (1996), URL <https://link.aps.org/doi/10.1103/PhysRevLett.77.1496>.
- [27] D. H. Froula, S. H. Glenzer, N. C. Luhmann, and J. Sheffield, eds., *Index* (Academic Press, Boston, 2011), second edition ed., ISBN 978-0-12-374877-5, URL <http://www.sciencedirect.com/science/article/pii/B9780123748775000208>.
- [28] J. S. Pearlman and R. L. Morse, Phys. Rev. Lett. **40**, 1652 (1978), URL <https://link.aps.org/doi/10.1103/PhysRevLett.40.1652>.
- [29] P. Mora, Phys. Rev. Lett. **90**, 185002 (2003), URL <https://link.aps.org/doi/10.1103/PhysRevLett.90.185002>.
- [30] A. V. GUREVICH, Sov. Phys.-JETP **22**, 449 (1989).
- [31] A. Decoster, P. A. Markowich, B. Perthame, and P.-A. Raviart, *Modeling of collisions*, vol. 2 (Elsevier, 1998).
- [32] M. M. Marinak, G. D. Kerbel, N. A. Gentile, O. Jones, D. Munro, S. Pollaine, T. R. Dittrich, and S. W. Haan, Physics of Plasmas **8**, 2275 (2001).
- [33] L. F. B. Hopkins, S. L. Pape, L. Divol, N. B. Meezan, A. J. Mackinnon, D. D. Ho, O. S. Jones, S. Khan, J. L. Milovich, J. S. Ross, et al., Physics of Plasmas **22**, 056318 (2015).
- [34] D. T. Casey, C. A. Thomas, K. L. Baker, B. K. Spears, M. Hohenberger, S. F. Khan, R. C. Nora, C. R. Weber, D. T. Woods, O. A. Hurricane, et al., Physics of Plasmas **25**, 056308 (2018), <https://doi.org/10.1063/1.5019741>, URL <https://doi.org/10.1063/1.5019741>.
- [35] L. B. Hopkins, S. LePape, L. Divol, A. Pak, E. Dewald, D. D. Ho, N. Meezan, S. Bhandarkar, L. R. Benedetti, T. Bunn, et al., Plasma Physics and Controlled Fusion **61**, 014023 (2018), URL <https://doi.org/10.1088%2F1361-6587%2Faad97e>.